Thin film Ag superlens towards lab-on-a-chip integration

Jeppesen, Claus; Nielsen, Rasmus Bundgaard; Boltasseva, Alexandra; Xiao, Sanshui; Mortensen, Asger; Kristensen, Anders

Published in:
Optics Express

Link to article, DOI:
10.1364/OE.17.022543

Publication date:
2009

Document Version
Publisher's PDF, also known as Version of record

Thin film Ag superlens towards lab-on-a-chip integration

C. Jeppesen,[1] **R. B. Nielsen,**[2] **A. Boltasseva,**[2] **S. Xiao,**[2]
N. A. Mortensen,[2] **and A. Kristensen**[1]

[1]*Department of Micro and Nanotechnology, Technical University of Denmark, DTU Nanotech, DTU-building 345 east, DK-2800 Kongens Lyngby, Denmark*
[2]*Department of Photonics Engineering, Technical University of Denmark, DTU Fotonik, DTU-building 345 west, DK-2800 Kongens Lyngby, Denmark*

anders@mailaps.org

Abstract: A thin metal film near-field superlens, as originally suggested by Pendry and realized by Fang *et al.* and Melville *et al.*, is investigated with emphasis on materials suitable for integration on a lab-on-a-chip platform. A chemically resistant cyclo-olefin copolymer (COC), mr-I-T85 from microresist technology, is applied as dielectric matrix/spacer for an Ag thin film superlens. The superlens successfully resolves 80 nm half-pitch gratings when illuminated with UV radiation at a free space wavelength of 365 nm. The superlens design, fabrication and characterization is discussed.

OCIS codes: (250.5403) Plasmonics, (220.0220) Optical design and fabrication, (220.4241) Nanostructure fabrication

References and links

1. J. B. Pendry and D. R. Smith, "Reversing light with negative refraction," Phys. Today **57**, 37 – 43 (2004).
2. J. B. Pendry, "Negative refraction makes a perfect lens," Phys. Rev. Lett. **85**, 3966 – 3969 (2000).
3. N. Fang, H. Lee, C. Sun, and X. Zhang, "Sub-diffraction-limited optical imaging with a silver superlens," Science **308**, 534 – 537 (2005).
4. D. O. S. Melville and R. J. Blaikie, "Super-resolution imaging through a planar silver layer," Opt. Express **13**, 2127 – 2134 (2005).
5. V. M. Shalaev and M. I. Stockman, "Optical properties of fractal clusters (susceptibility, surface enhanced Raman scattering by impurities)," Sov. Phys. JETP **65**, 509–522 (1987).
6. Z. T. Liu, M. D. Thoreson, A. V. Kildishev, and V. M. Shalaev, "Translation of nanoantenna hot spots by a metal-dielectric composite superlens," Appl. Phys. Lett. **95**, 033114 (2009).
7. R. Holt and T. Cotton, "Surface-enhanced resonance Raman and electrochemical investigation of Glucose oxidase catalysis at a silver electrode," J. Am. Chem. Soc. **111**, 2815–2821 (1989).
8. M. Yang, F. Chung, and M. Thompson, "Acoustic network analysis as a novel technique for studying protein adsorption and denaturation at surfaces," Anal. Chem. **65**, 3713–3716 (1993).
9. K. Brown, A. Fox, and M. Natan, "Morphology-dependent electrochemistry of cytochrome c at Au colloid-modified SnO2 electrodes," J. Am. Chem. Soc. **118**, 1154–1157 (1996).
10. T. A. P. GmbH, "TOPAS Advanced Polymers," www.topas.com (2009).
11. R. R. Lamonte and D. McNally, "Uses and processing of cyclic olefin copolymers," Plast. Eng. **56**, 51–55 (2000).
12. O. Gustafsson, K. B. Mogensen, and J. P. Kutter, "Underivatized cyclic olefin copolymer as substrate material and stationary phase for capillary and microchip electrochromatography," Electrophoresis **29** (2008).
13. M. J. Weber, *Handbook of optical materials* (CRC Press, Boca Raton, 2003).
14. M. Scholer and R. J. Blaikie, "Simulations of surface roughness effects in planar superlenses," J. Opt. A: Pure Appl. Opt. **11**, 105503 (2009).
15. H. Lee, Y. Xiong, N. Fang, W. Srituravanich, S. Durant, M. Ambati, C. Sun, and X. Zhang, "Realization of optical superlens imaging below the diffraction limit," New J. Phys. **7**, 255 (2005).
16. P. Chaturvedi, K. Hsu, S. Zhang, and N. Fang, "New frontiers of metamaterials: design and fabrication," MRS Bull. **33**, 915 – 920 (2008).

#117515 - $15.00 USD Received 21 Sep 2009; revised 21 Nov 2009; accepted 23 Nov 2009; published 24 Nov 2009

17. L. Vj, N. P. Kobayashi, M. S. Islam, W. Wu, P. Chaturvedi, N. X. Fang, S. Y. Wang, and R. S. Williams, "Ultrasmooth Silver Thin Films Deposited with a Germanium Nucleation Layer," Nano Lett. **9**, 178–182 (2009).

1. Introduction

The diffraction limit is traditionally considered to impose a fundamental obstacle for optical imaging of nanometer scale objects and macro-molecules. The emergence of metamaterial concepts is challenging this classical prejudice [1] — in particular, the superlens, as originally proposed by Pendry [2]. A flat silver slab interfaced with a dielectric layer that has a matching real part of the relative permittivity ($\varepsilon_{\text{metal}} = -\varepsilon_{\text{dielectric}}$) can serve as a superlens in the UV to IR region. Such a lens can image objects in the near-field below the classical diffraction limit. As an example Fang *et al.* [3] demonstrated near-field imaging resolving 60 nm features using UV radiation at a vacuum wavelength of 365 nm. Fang's superlens structure consisted of a quartz wafer, a focused ion beam (FIB) written grating pattern in a 50 nm Cr film, a 40 nm polymethyl-methacrylate (PMMA) spacer layer, a 35 nm thick Ag film, and finally 100 nm of the negative photoresist NFR105G. The image of the grating structures was recorded in the photoresist by UV-exposure - at wavelength 365 nm - through the grating and the thin film superlens, see Fig. 1. The exposure took place using a standard I-line aligner and they managed to resolve 60 nm half-pitch (Λ) gratings corresponding to features of the order $\lambda/6$. Almost simultaneously Melville *et al.* [4] demonstrated near-field superlensing by employing the same lithography readout mechanism.

These investigations have focused on demonstrating the sub-wavelength imaging capabilities and exploring their fundamental nature rather than actual applications of such devices. The non-invasive nature of optical probing is inherently attractive in biotechnology and lab-on-a-chip. One such application could be spatial translation of localized electromagnetic fields, also known as "hot spots" [5] for enhanced flourescence microscopy. Hot spots are produced by metal nanoantennas and can be used in sensing applications including surface-enhanced Raman scattering (SERS) and enhanced fluorescence microscopy [6]. The field enhancement is inversely proportional to the distance between the nanoantennas and the fluorophores. Direct contact, however, might result in undesirable structural or functional changes of the biomolecules [7] such as the denaturation of proteins [8, 9]. This can be avoided by using a Ag near-field superlens to transfer the "image" of the hot spots to the biomolecules, thereby enabling a spatial distance between the nanoanteannas and the molecules. In this way chemical interaction, between the biomolecules and the antenna is suppressed. This motivates our investigations of superlens concepts in lab-on-a-chip systems, reported in this paper. We therefore consider the choice of materials, which should be compatible with the down-stream micro-fabrication steps, required to integrate the superlens with micro and nanofluidic components in a lab-on-a-chip.

In comparison to Fang's device [3], we have replaced PMMA by a likewise biocompati-

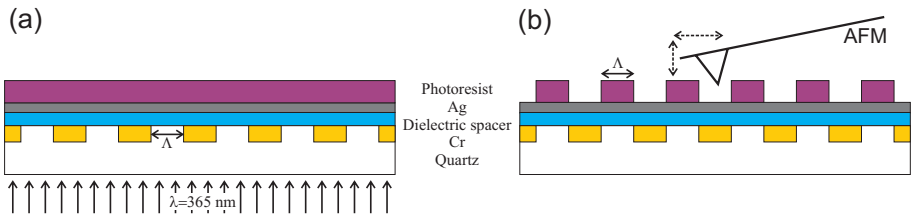

Fig. 1. Near-field superlens design using UV-lithography readout. (a) Exposure of negative photoresist through the quartz/Cr mask and the Ag superlens of a grating pattern with period 2Λ. (b) AFM scan of the exposed and developed photoresist.

#117515 - $15.00 USD Received 21 Sep 2009; revised 21 Nov 2009; accepted 23 Nov 2009; published 24 Nov 2009

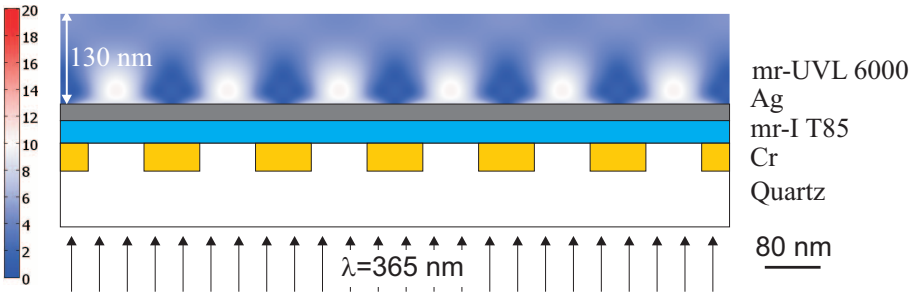

Fig. 2. Finite element simulation of the intensity-distribution $(|E|/|E_0|)^2$ for six grating periods illuminated by 365 nm radiation. The grating has a half-pitch of 80 nm.

ble, but highly chemical resistant cyclic-olefin copolymer (COC) called mr-I T85. The relative permittivity of mr-I T85 is $\varepsilon_{\mathrm{T85}} = 2.415$ at 365 nm and thereby matches the value of silver ($\varepsilon_{\mathrm{Ag}} = -2.401$) better than that of PMMA ($\varepsilon_{\mathrm{PMMA}} = 2.301$). Compared to PMMA, COC based materials are more heat resistant, have a lower water absorption, and are more chemically resistant [10, 11]. COC materials have demonstrated superior transmission in the UV region [10], thereby enabling absorption measurements in lab-on-a-chip systems at λ=254 nm [12]. These combined properties make COC materials far more suitable than PMMA for lab-on-a-chip applications. Due to the well matching permittivities of silver and mr-I T85, mr-I T85 was preferred compared to common dielectrics such as SiO_2 ($\varepsilon_{\mathrm{SiO_2}} = 2.25$ [4]) or Al2O3 ($\varepsilon_{\mathrm{Al_2O_3}} = 3.217$ [13]).

In addition are a different photoresist, the mr-UVL 6000 ($\varepsilon_{mr6000} = 2.719$) and the patterns are e-beam written instead of FIB written. Furthermore, the chrome pattern is embedded into the quartz wafer to ease the planarization process. In the following, the design considerations and fabrication issues are discussed together with the optical performance of the COC based superlens devices.

2. Design considerations

To support our design of the grating structure we take advantage of full-wave simulations of the transmitted field. We employ a commercially available finite-element method (Comsol Multiphysics) which solves the wave equation, Eq. 1

$$\nabla \times \nabla \times E = \frac{\omega^2}{c^2} \varepsilon E, \tag{1}$$

with an incident electrical field E_0 polarized perpendicular to the grading lines. The system is depicted in Fig. 2 where we apply perfectly-matched layers (PMLs) for the horizontal domain boundaries while periodic boundary conditions are employed for the vertical domain boundaries. The figure shows the intensity-distribution $(|E|/|E_0|)^2$ for 365 nm radiation normally incident on a half-pitch of Λ=80 nm. For the material properties we employ $n = 1.475$ for the quartz, $n = 1.40 + i3.25$ for Cr, $n = 0.407 + i4.43$ for Al, $n = 1.554$ for mr-I T85 corresponding to $\varepsilon = 2.415$, $\varepsilon = -2.401 + i0.2488$, and $n = 1.649$ for mr-UVL 6000. The different length scales correspond to those of the fabricated structure, as discussed in the fabrication section.

In Fig. 2, the intensity distribution shows six ”peaks” that can be associated with the six windows in the chrome mask. If the peaks are given an above-threshold dose, some residual layer exposure is to be expected. In Fig. 3(a)-(c) we summarize further modeling of structures with different grating periods, Λ=60-80 nm.

#117515 - $15.00 USD Received 21 Sep 2009; revised 21 Nov 2009; accepted 23 Nov 2009; published 24 Nov 2009

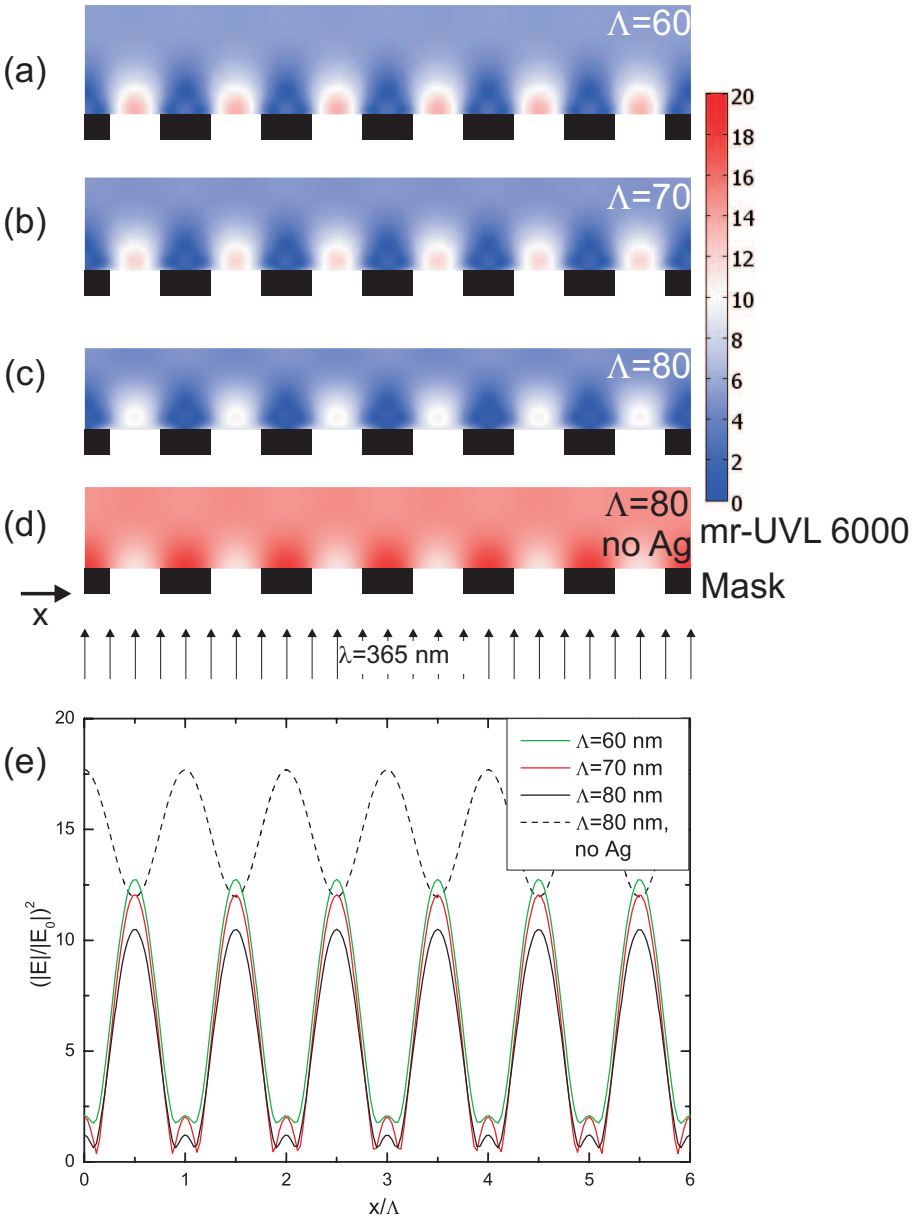

Fig. 3. Finite-element modeling of the intensity-distribution $(|E|/|E_0|)^2$ above the superlens when illuminated through gratings of different period. To simplify the plot and ease comparison, the mr-I T85 and the silver layers are not depicted. Panels (a)-(c) are with Λ=60, 70, and 80 nm and a silver superlens film. Panel (d) is a reference with Λ=80 nm where the 35 nm Ag layer has been replaced by 35 nm of mr-I T85. Panel (e) is the intensity cross-section 15 nm into the resist as a function of the normalized position x with respect to the grating period Λ.

#117515 - $15.00 USD Received 21 Sep 2009; revised 21 Nov 2009; accepted 23 Nov 2009; published 24 Nov 2009

As the period increases, the six intensity peaks in the resist are gradually smeared out illustrated by the slight decrease in contrast. We emphasize that for the particular design of the grading structure, the 80 nm grating is the largest period where six individual peaks are easily identifiable. For demonstration purposes we have thus pursued a silver superlens design which is able to resolve features corresponding to a grating with an 80 nm half-pitch. As a control structure, Fig. 3(d) illustrates the situation where the silver is replaced by mr-I T85. The six peaks are visible but the contrast is poor compared to the silver superlens, see Fig. 3(e). The high intensity peaks are positioned in front of the mask instead of the mask openings contrary to Fig. 3(a)-(c). This indicates that without the silver film we obtain a diffraction pattern.

3. Fabrication

The fabrication, see Fig. 4, can be split into two parts: The fabrication of the mask and the fabrication of the superlens stack. A 100 nm ZEP520A (3.6%, Zeon Corp., Tokyo, Japan) layer is spincoated onto a 1 mm fused silica substrate. Subsequently, a 15 nm aluminium layer is thermally deposited on top of the ZEP layer to prevent charge accumulation during the following electron beam lithography (EBL) step. The proximity corrected EBL exposure is done with a 100 kV JEOL JBX-9300FS EBL tool (120 μC/cm^2 dose, 0.6 nA current, 4 nm spot-size). The pattern consists of 30$\times$30 μm areas of 70-120 nm half-pitch gratings and 30-150 nm isolated lines. The aluminium layer is removed in 1 min of undiluted MF-322 (Rohm and Haas, Coventry, UK) and the positive ZEP resist is developed 1 min in ZED-N50 (Zeon Corp.) developer followed by an IPA rinse. Then a brief descum process (asher, 5 min, 70 sccm O2, 70 sccm N2, 150 W) is carried out to remove any residual resist. Subsequently, a reactive ion etching (RIE, 1 min 40 s, 24 sccm CF4, 42 sccm CHF3, 24 W, 16 mTorr) process is used to etch 50 nm into the glass. 50 nm Cr is then embedded into the fused silica by electron beam deposition and the wafer is immersed into Remover 1165 (Rohm and Haas) with ultrasound for 2 hours, which dissolves the ZEP layer. Embedding the Cr mask ensures a more even surface and thereby simplifies the later planarization process. The wafer is placed in a HMDS-oven and 1.5 μm of positive photoresist AZ5214e is spincoated on. The wafer is exposed in an I-line aligner with a dose of 70 mJ/cm^2 through a mask with 20$\times$20 μm windows and subsequently developed. A 50 nm Al cover is thermally deposited to block all light that does not go through the quartz/chrome mask from reaching the mr-UVL 6000 layer. This is to minimize waveguiding in the photoresist during the exposure. The AZ5214e layer is removed in acetone, which marks the conclusion of the mask structure, see Fig. 5.

The height of the Al layer is then measured by AFM. The next step is the superlens stack, which consists of a 40 nm mr-I T85 planarization layer, a 35 nm Ag layer and 70 nm mr-UVL 6000. The thickness of the mr-UVL 6000 is chosen to minimize waveguiding within the resist. First 300 nm mr-I T85 is spincoated onto the wafer, etched in the RIE (2 min, 20 sccm O2, 99 sccm N2, 20 W), given a 1 min oxygen plasma (asher) to planarize the surface and to reflow the mr-I T85. The thickness of the mr-I T85 layer is measured by ellipsometry and the profile across the mask areas is measured. By combining this information with the height of the aluminium layer and the etch rate, the remaining etch time can be estimated. The wafer is RIE etched again and given 1 min oxygen plasma. The thickness is measured by ellipsometry to 40 nm$\pm$2.5 nm and the roughness Rq over a 5$\times$5 μm area is 0.5 nm. Then 35 nm of Ag is deposited by e-beam deposition at a rate of 1.5 Å/s and 70 nm of mr-UVL 6000 is spincoated on top. The Rq roughness of the Ag layer is 0.8 nm, see Fig. 6. Spincoating of mr-UVL 6000 concludes the fabrication process.

#117515 - $15.00 USD Received 21 Sep 2009; revised 21 Nov 2009; accepted 23 Nov 2009; published 24 Nov 2009

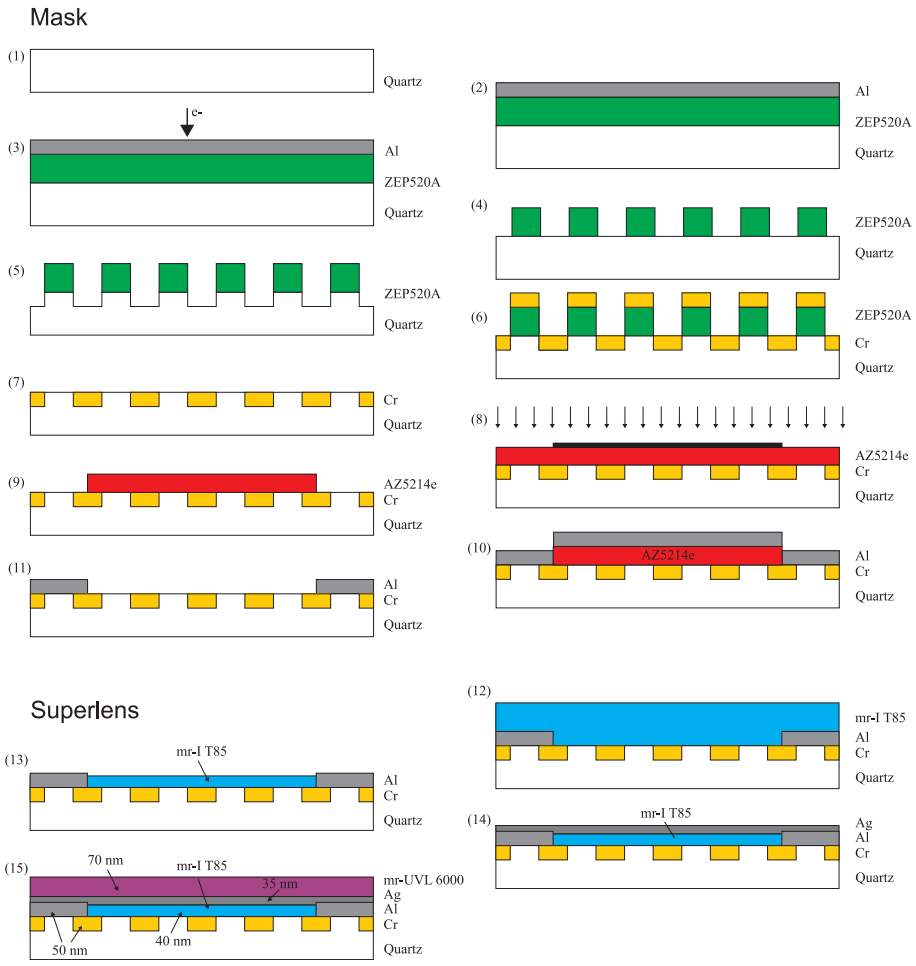

Fig. 4. Schematic drawing of the processflow. (1) Quartz wafer. (2) Spincoat of ZEP520A and deposition of Al. (3) EBL exposure. (4) Development. (5) RIE etch quartz. (6) Deposition of Cr. (7) Removal of ZEP520A. (8) UV-lithography of AZ5214e. (9) Development. (10) Al deposition. (11) Lift-off. (12) Spincoat mr-I T85. (13) RIE etch mr-I T85. (14) Ag deposition. (15) Spincoat mr-UVL 6000.

#117515 - $15.00 USD Received 21 Sep 2009; revised 21 Nov 2009; accepted 23 Nov 2009; published 24 Nov 2009

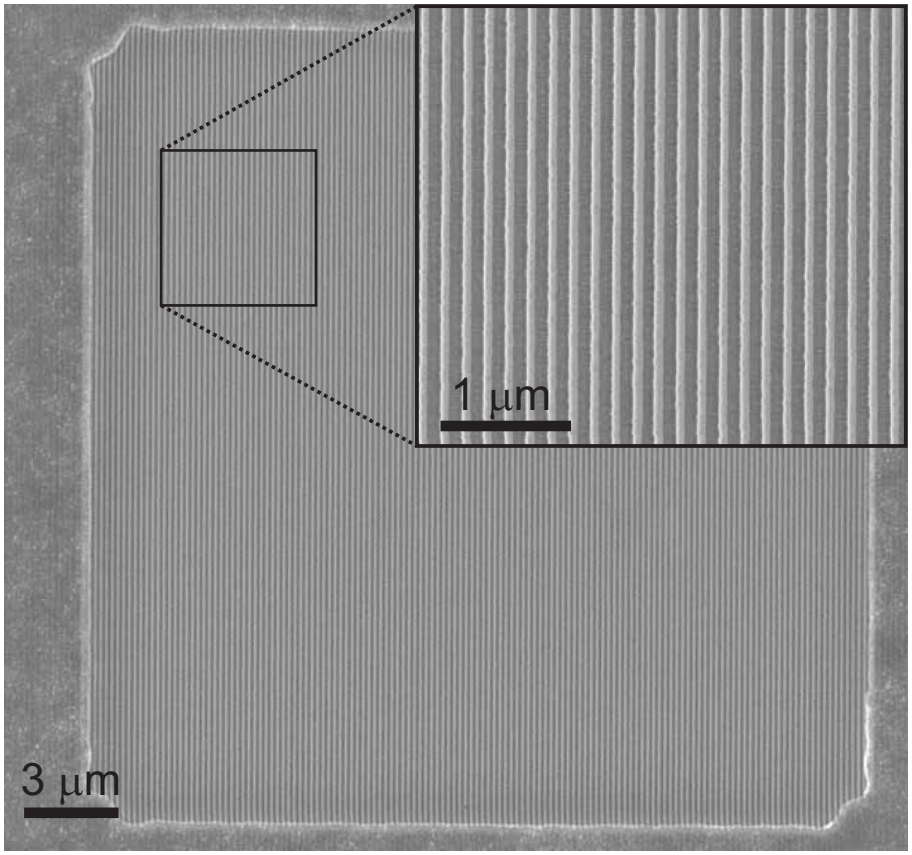

Fig. 5. SEM image of the 20×20 μm opening in the Al layer to the 80 nm half-pitch quartz/chrome gratings.

4. Results

The fabricated superlens devices were optically characterized by I-line (365 nm) UV flood exposure in a contact aligner applying a dose of 750 mJ/cm^2. After exposure, the mr-UVL 6000 was given a post exposure bake at 120°C for 5 min followed by a 50 s development step in Propylene Glycol Methyl Ether Acetate (PGMEA). The exposed and developed structures were then characterized by AFM, see Fig. 7. To verify that the periodic structure was indeed due to a superlensing effect, a control wafer was made where the silver layer was replaced by mr-I T85. This gives the same distance between the mask and the resist, but without the silver it should not be possible to reproduce the grating structure in the photoresist. The result can be seen in Fig. 7(b).

As seen in Fig. 7(a) and (c), the 80 nm half-pitch gratings are well reproduced in the photoresist. The image of the gratings is clearly of a lower quality than the original mask, see Fig. 6(a). This could indicate that the superlens was unable to restore all the Fourier components e.g. fast decaying high order components. Furthermore, photolithography represents an indirect and far from ideal readout mechanism of the incident light intensity where the resist's dose-response curve acts as the transfer function from the light intensity to the exposed resist. Additionally, the surface roughness of the silver has a large effect on the resolution and thereby image quality. The peak to valley distance in the AFM scan is only around 1 nm. Several factors may have

#117515 - $15.00 USD Received 21 Sep 2009; revised 21 Nov 2009; accepted 23 Nov 2009; published 24 Nov 2009

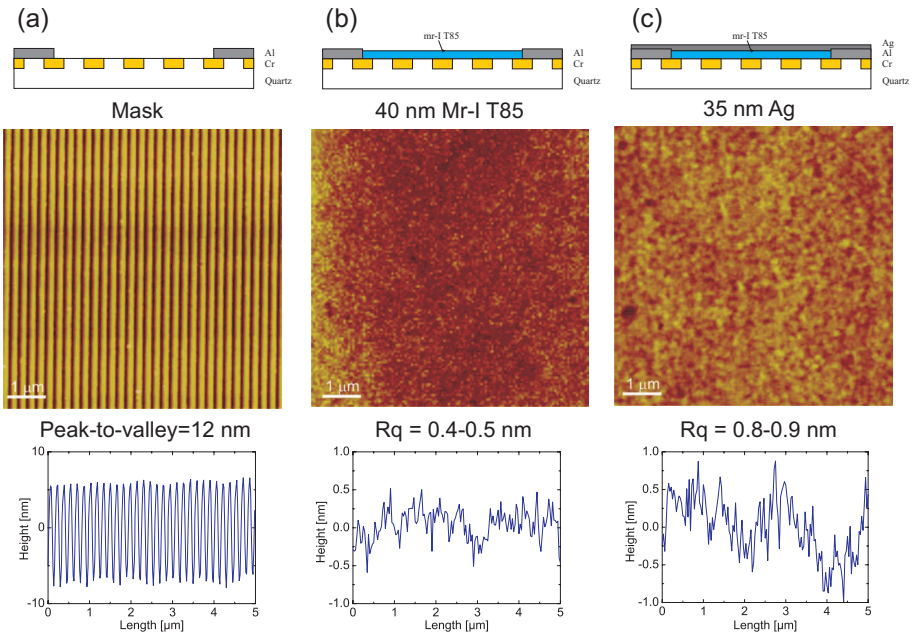

Fig. 6. The fabricated near-field superlens. AFM micrographs and surface profiler scans after different process steps: (a) Cr mask with 80 nm half-pitch on glass substrate. (b) Spin-coating and back-etch of 40 nm thick mr-I T85 film, which serves as dielectic matrix/spacer. A surface roughness Rq below 0.5 nm is achieved. (c) 35 nm Ag film, with a Rq below 0.9 nm.

contributed to this. AFM tip convolution can result in shallower valleys since the tip has a finite size and taper. A large contribution can also be ascribed to the residual layer exposure, which can be clearly seen in the simulations, see Fig. 2.

From the simulations it is expected that more than half of the resist height is a result of residual layer exposure assuming that the threshold of the resist is reached at half maximum of the intensity. Other factors relate to the chemical processes occurring in the resist during exposure, baking and development. Out of the different grating sizes, the 80 nm half-pitch gratings are the easiest to identify. Pattern defects are caused by height variations of the mr-I T85 layer and areas of higher surface roughness. For the 70 nm gratings the Ag roughness might be too large for the gratings to be properly resolved since there is an inverse proportionality between resolution and surface roughness [14, 15, 16]. The control wafer with 75 nm mr-I T85 instead of 40 nm mr-I T85 and 35 nm Ag shows no sign of image contrast, see Fig. 7(c). The missing grating structure evidently supports that the previous results were caused by enhancement of the evanescent field at the metal/dielectric interfaces due to surface plasmons. We measured the dose-response curve (retention height vs. exposure dose) and have used a dose corresponding to maximum slope on the dose curve. Although no systematic study was made, we have tested different doses around the maximum slope point. However, we did not observe any contrast improvements.

The evanescent wave has a characteristic decay length, Eq. 2 [15]

$$Z = \frac{1}{4\pi} \frac{1}{\sqrt{a^{-2} - \varepsilon\lambda^{-2}}}, \tag{2}$$

where a is the period and λ is the free space wavelength. In the present case we get 17 nm

#117515 - $15.00 USD Received 21 Sep 2009; revised 21 Nov 2009; accepted 23 Nov 2009; published 24 Nov 2009

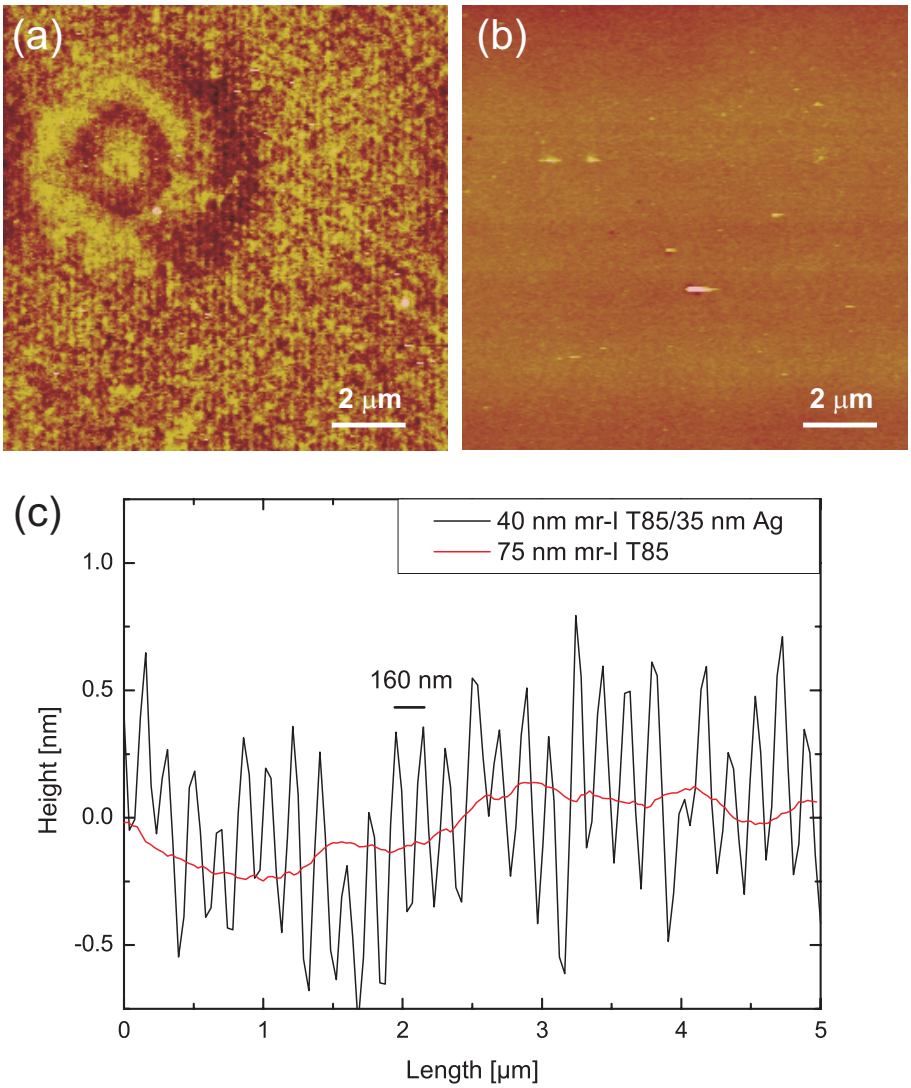

Fig. 7. (a) 8×8 μm AFM scan of the recorded image of 80 nm half-pitch gratings in the mr-UVL 6000 resist. The exposure was done through the Ag superlens. (b) 8×8 μm AFM scan of the obtained image of 80 nm half-pitch gratings in the resist where the Ag layer was replaced with mr-I T85. (c) Height scan of the images (a) and (b).

#117515 - $15.00 USD Received 21 Sep 2009; revised 21 Nov 2009; accepted 23 Nov 2009; published 24 Nov 2009

so that the field intensity is reduced to $1/e = 0.37$ of its original value within the first 17 nm beyond the mask. After 75 nm the intensity of the evanescent wave is therefore expected to be minor. An advantage of embedding the structure is that a single mr-I T85 layer can be used for planarization but also that the dielectric planarization layer can be reduced in thickness. According to Lee *et al.* [15], a thinner spacer layer than the 40 nm would drastically increase the transmissivity of evanescent waves. Initial tests have shown that the mr-I T85 thickness can be reduced below 40 nm without compromising the surface roughness. 30 nm spacer layers should be possible, which should improve the quality of the recorded image significantly. Recent developments in Ag deposition can further improve the image quality [17].

5. Conclusion

We have demonstrated superlensing by reproducing a 80 nm half-pitch grating structure in a negative photoresist using 365 nm vacuum wavelength UV radiation. The results were supported by finite-element modeling of the field-distribution in the resist. With the current materials the superlens is suitable for integration in nanofluidic systems but further optimization and initial tests on arbitrary objects should be carried out in advance.

The integrated silver superlens will provide all the advantages of surface enhanced spectroscopy without having the sample molecules in the vicinity of the metal surfaces causing the field enhancement. As examples, the microfluidic device with integrated thin film superlens and plasmonic nanoantennas, will enable field enhanced remote probing of biomolecules without pertubing the electrochemical environment of the suspended biomolecules. The lab-on-a-chip with integrated superlens therefore has high potential impact on chip based protein detection, where the remoteness of lens and nanoantennas may prevent undesirable structural or functional changes of the biomolecules such as the denaturation of proteins.

Acknowledgments

This work is financially supported by The Danish Research Council for Technology and Production Sciences (grants no. 274-07-0057 and 274-07-0379).

#117515 - $15.00 USD Received 21 Sep 2009; revised 21 Nov 2009; accepted 23 Nov 2009; published 24 Nov 2009